AIAA JOURNAL
Vol. 34, No. 7, July 1996

Modeling of Dust Entrainment by High-Speed Airflow

M. Richard Denison* and Philip A. Hookham†
Titan Corporation, Chatsworth, California 91311

An analytical model for dust lofting due to shock waves or high speed (>100 fps) winds is described. The model divides the dusty boundary layer into two rigions, an inner granular flow region where particle impacts dominate and an outer region where turbulent diffusion dominates. The two regions are linked by specifying appropriate boundary conditions at a matching point. The effect of surface cohesion is modeled with a parameter representing the energy necessary to fluidize the surface material. The model has been implemented into the MAZe (multiphase adaptive zoning) hydrocode. As a validation of the model, the code was used to simulate a wind-tunnel dust lofting experiment. The model produced good agreement with experimental mass lofting rates and vertical dust loading profiles.

Nomenclature

C = constant for scale; see Eq. (14)
$c_4(e)$ = $F4/F3^2$ (see the Appendix)
DH = $\Delta H_v/u_e^2$
d = particle diameter
e = coefficient of restitution
$F_i(e)$ = see Appendix
k = turbulent kinetic energy
l = turbulent scale
m_p = particle mass
$\dot{m}_d$ = diffusion mass flux; see Eq. (1)
$\dot{m}^*$ = dimensionless mass flux; see Eq. (15)
q_k = flux of turbulent kinetic energy
q_p = particle heat flux
T_p = particle fluid energy; see Eq. (27)
T_p^* = particle fluid temperature
t = time
u = streamwise velocity
u_τ = shear velocity
v = normal velocity
x = streamwise distance
y = normal distance
γ = inelastic energy loss
ΔH_v = energy of fluidization
δ = boundary-layer thickness
η = see the Appendix
κ = ratio of particle to air density
μ = particle viscosity; see Eq. (27)
ν = turbulent eddy viscosity; see Eq. (1)
υ = ratio of particle density to particle specific gravity; see the Appendix
ρ = air density
ρ_p = particle density
ρ_s = particle specific gravity
$\bar{\rho}$ = mean density; see Eq. (1)
σ_k = turbulent Prandtl number
σ_κ = turbulent Schmidt number
τ = turbulent shear stress; see Eq. (1)
τ_p = particle fluid shear stress; see Eq. (2)

I. Introduction

THE sweep-up of dust and other debris by a nuclear blast wave provides the source for nuclear dust clouds. Since the size and composition of nuclear dust clouds is important to military planners who must consider such problems as reentry vehicle fratricide and aircraft dust ingestion, the mechanism of dust sweep-up is of interest. Entrainment of dust/debris also has other potential military and nonmilitary applications, such as collateral effects due to strikes on facilities containing chemical or biological weapons and volcanic eruptions.

Computational fluid dynamics (CFD) codes that model the formation of nuclear dust clouds lack the spatial resolution and physical models to simulate the entrainment of dust directly. The hydrocode computational grid is never fine enough to completely resolve the thin area near the soil surface where dust sweep-up occurs, and these codes do not solve the appropriate equations for simulating the flow of dust in high concentration (i.e., granular flow). Therefore, a subgrid model is necessary for modeling the entrainment of dust.

Previous models[1,2] have emphasized lofting of incohesive (dry, loose) soils on the assumption that they would maximize lofting, thereby providing an upper bound for dust mass in dust clouds. Realistic terrain is composed of many soil types, however, including cohesive soils, vegetation cover, clods, snow, etc., which may have substantially different lofting characteristics than incohesive soils. The current model was therefore designed to include a framework whereby the lofting of realistic soils could be modeled.

A simple method for modeling the subgrid region that became popular several years ago was the dusty law of the wall. This method (see, for example, Ref. 1) was developed as a substitute, when dust is present, for the well-known log law profiles of a turbulent boundary layer. Although the law of the wall method has the advantage of simplicity, it is not obvious that new experimental observations and the emphasis on real surfaces can be dealt with in this method. Furthermore, even in the case of loose dry sand, it appears that the influence of a fluidized layer of high dust density close to the ground should be included in the model. An attempt to deal with the fluidized layer as well as the outer turbulent flow, called a two layer model, was developed in Ref. 2. In this paper that model is improved and modified to account for real surface effects.

The objectives of this dust sweep-up analysis are 1) to develop a method for calculating the dust lofting over real surfaces in a high-speed airflow, 2) to validate model predictions with recent wind-tunnel experiments, and 3) to develop a practical method for implementing the subgrid lofting model in a hydrocode.

II. Model Formulation

The model features are illustrated in Fig. 1. The edge of the dusty boundary layer represents the outer extent of the region where the surface directly influences the flow. As will be seen later, the edges of the dust and velocity layers do not coincide exactly. The outer turbulent region contains dust, but the dust density is sufficiently low that collisions between particles are rare. The mechanism of transport is dominated by turbulence. A mean kinetic energy k of random fluctuations is a characteristic of the turbulence. In the inner fluidized layer, particle densities are so high that particles cannot

Received April 19, 1995; presented as Paper 95-2206 at the AIAA 26th Fluid Dynamics Conference, San Diego, CA, June 19–22, 1995; revision received Aug. 10, 1995; accepted for publication Aug. 24, 1995.

*Consultant. Member AIAA.
†Senior Research Scientist, Research and Technology Division. Member AIAA.

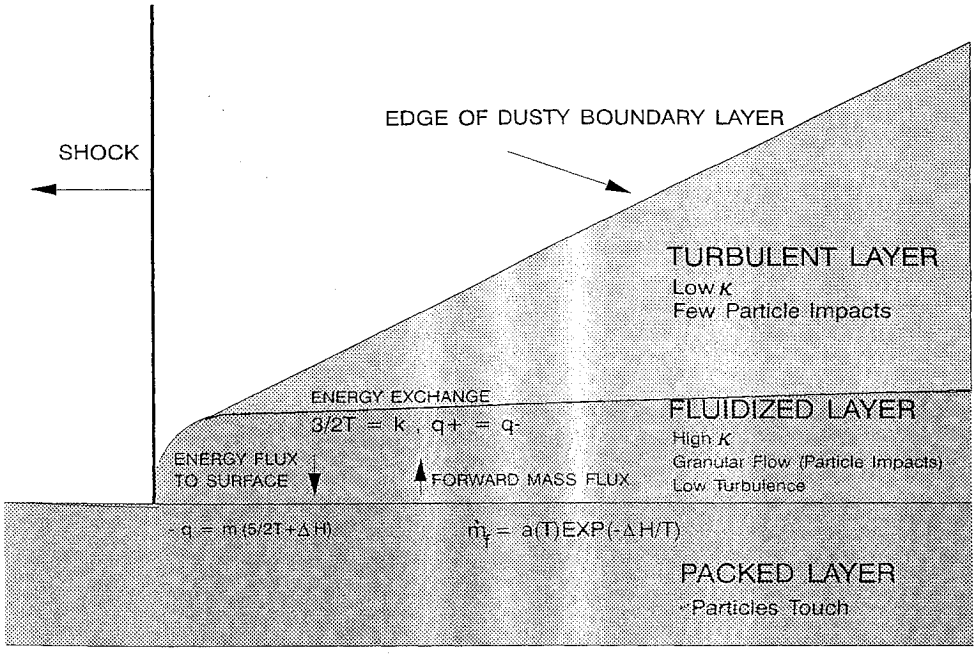

Fig. 1 Model features.

avoid colliding with each other. Transport in this region is dominated by the granular flow that behaves much like a laminar fluid. Energy is exchanged from the outer turbulence to the fluidized region to produce a random energy due to collisions that may be thought of as a particle temperature. Because of the large mass difference between the colliding particles and the gas molecules, this temperature is not in equilibrium with the gas temperature. This energy is in turn transported to the surface of the packed layer where the particles touch. The disturbance of the packed layer eventually leads to the mechanism of dust lofting or sweep-up characterized by an energy of fluidization, ΔH_v, analogous to a heat of vaporization, which is introduced to help account for soil properties and to correlate the model with experiments.

Comparison with experiments is essential. At the present stage of development, the fluid dynamics cannot be developed entirely from first principles. A small number of physical parameters must be determined from data. Moreover, the model must be capable of predicting gross features such as dust lofting rate and layer thickness as well as detailed boundary-layer profiles.

The recent wind-tunnel experiments of Batt et al.[3] gave a great deal more detail with considerably less scatter in the data than the previous shock tube results,[4,5] although the wind velocities are at the lower end of the range of interest. One of the striking features observed in the data was a very strong decay in mass lofting with axial distance. This is consistent with previous predictions in Refs. 1, 2, and 6. However, this scaling was not universally expected.[7-9] The results of recent experiments with real surfaces[16] were not available at the time of this study.

III. Subgrid Model

The subgrid model makes use of the observation that in turbulent boundary layers transport across streamlines is stronger than advection effects. Therefore, profiles in both the fluidized layer and the turbulent layer can be deduced in terms of physical parameters by neglecting advection and treating the conservation relations as a Couette flow. After boundary and matching conditions are imposed, all variables are found in terms of a single dimensionless parameter that can be related to position through use of the momentum integral equation. To complete the model three constants must be found from experimental data: the effective particle size, a turbulent Schmidt number, and a damping factor for the dusty flow. After these constants are found, the required parameters and integrals are curvefit in terms of normalized boundary-layer thickness, δ/d, and fluidization energy, $DH(\Delta H_v/u_e^2)$ for use in the hydrocode.

The conservation equations are written under the assumption that there is negligible velocity difference between the gas and the particles. The experiments of Batt et al.[3] indicate that this is a reasonable assumption for the particle sizes they used. The transport relations for mass, momentum, and flux of turbulent kinetic energy in the outer turbulent portion of the boundary layer are as follows, where $\bar{\rho} = \rho(1+\kappa)$ and $\nu = lk^{1/2}$:

$$\dot{m}_d = -\frac{\bar{\rho}\nu}{\sigma_\kappa(1+\kappa)}\frac{\partial \kappa}{\partial y}, \qquad \tau = \bar{\rho}\nu\frac{\partial u}{\partial y}, \qquad -q_k = \frac{\bar{\rho}\nu}{\sigma_k}\frac{\partial k}{\partial y} \tag{1}$$

The conservation equations for the thin fluidized region above the packed layer are assumed to be dominated by the particles. Interactions with the gas are neglected. The transport relations for momentum, energy, inelastic energy loss, and equation of state in the fluidized region are given by

$$\tau_p = \rho_s\, \mathrm{d}T_p^{\frac{1}{2}} F_1(e)\frac{\partial u_p}{\partial y}, \qquad -q_p = \rho_s\, \mathrm{d}T_p^{\frac{1}{2}} F_2(e)\frac{\partial T_p}{\partial y}$$
$$\gamma = c_4(e)P_p^2/\rho_s T_p^{\frac{1}{2}}\,\mathrm{d}, \qquad P_p = \rho_p T_p \tag{2}$$

The terms F_1, F_2, and c_4 are all functions of the coefficient of restitution e. Analytic expressions for these functions taken from the kinetic theory developed by Lun et al.[10] are given in the Appendix. It has been assumed that in the fluidized layer the ratio ϱ_p/ϱ_s is small so that expressions analogous to those of a perfect gas result. The use of T_p that has the units of velocity squared has become conventional in the granular flow literature. It is related to the temperature T_p^* associated with the random motions of the particles caused by collisions:

$$T_p = kT_p^*/m_p \tag{3}$$

where k is the Boltzmann constant. The particle internal energy and enthalpy are

$$e_p = \tfrac{3}{2}T_p, \qquad h_p = \tfrac{5}{2}T_p \tag{4}$$

With the use of the equation of state and the definition of enthalpy, the three particle conservation equations are supposed to determine the four variables u_p, v_p, ρ_p, and T_p. The normal momentum equation could be used to supply the missing relationship, but it is simpler to invoke the usual boundary-layer assumption that the pressure is constant across the thin fluidized layer. Since the momentum and energy equations are second order, a total of five boundary conditions

are required for the fluidized layer. Six matching conditions at the turbulent region interface and two boundary conditions at the packed layer surface satisfy the required number of boundary conditions.

The matching conditions at the interface are taken to be as follows:

$$y = y_m; \qquad \kappa^+ = \kappa^-, \qquad u^+ = u_p^-, \qquad k^+ = e_p^-$$
$$q_k^+ = q_p^-, \qquad \tau^+ = \tau_p^-, \qquad \dot{m}_d^+ = (\rho_p v_p)^- \tag{5}$$

The superscript + indicates the turbulent side of the interface and − is the granular side. The turbulent kinetic energy is identified with the particle internal energy at the interface. Although both quantities are averages of random fluctuations, one is caused by turbulence, whereas the other is caused by particle impacts. The energy fluxes and shear stresses are also equated, although these also depend upon different phenomena in the two regions. Finally, the vertical transport is assumed to be dominated by diffusion in the turbulent region, but vertical mean velocity is the mechanism in the fluidized region.

At the interface between the fluidized layer and the packed layer two more conditions are required:

$$\dot{y} = 0; \qquad u_p = l_p \frac{\partial u_p}{\partial y}, \qquad -q_p = \dot{m}(h_p + \Delta H_v) \tag{6}$$

where $l_p = \rho_s d/6\rho_p$. The first condition allows for slip flow analogous to rarefied gas flow. Usually this velocity is small compared with the freestream velocity but under conditions of low particle density at the surface slip can become important. To be consistent with the slip flow condition a jump in enthalpy between the packed layer and the fluidized layer should be modeled, but in the interest of simplicity this will be ignored. Low mean free path at this interface rarely occurs for conditions of interest. The second condition is a steady-state ablation condition. It states that the energy conducted out of the fluidized layer is just sufficient to yield the outward flux of energy at the interface. The energy flux contains a part associated with the sensible heat plus the energy required to fluidize the particles. This energy might be related to overcoming cohesive forces or just energy required to become free of the packed layer. It is analogous to the heat of vaporization for a solid material.

The set of boundary conditions that have been introduced would be sufficient if the location of the matching point between the fluidized layer and the turbulent layer were known either by means of a physical criterion or empirical observation. In the previous work[2] a fixed value of κ was chosen that served to define the matching point. In the present investigation this condition is relaxed in favor of an additional analogy with molecular substances at the surface of the packed layer. The net mass flux at the surface is a balance between a flux leaving the surface $\dot{m}_f$ and the flux striking the surface $\dot{m}_b$:

$$\dot{m} = \dot{m}_f - \dot{m}_b \tag{7}$$

The flux striking the surface is given by

$$\dot{m}_b = mn\bar{c}/4 = P_p/\sqrt{2\pi T_p} \tag{8}$$

In equilibrium the forward and backward rates are equal. Under these conditions the pressure of the fluidized layer is related to the surface temperature through integration of Clapeyron's equation:

$$(P_p)_{eq} = A\exp(-\Delta H_v/T_p) \tag{9}$$

For molecular substances the constant of integration A is determined by means of statistical mechanics. For this analysis the results for vaporization of a crystalline solid are carried over directly to define the constant. If the sticking factor is unity, the forward flux that approaches equilibrium smoothly with the backward flux is given by

$$\dot{m}_f = A\exp(-\Delta H_v/T_p)/\sqrt{2\pi T_p} \tag{10}$$

The outer edge will be assumed to be an ideal flow (uniform for the wind-tunnel case) for purposes of developing the subgrid model. Therefore, at the outer edge of the boundary layer u_e and κ_e are assumed to be known.

IV. Couette Flow Profiles

Profiles of velocity, particle density, particle energy, and turbulence properties are determined in terms of physical parameters by means of Couette flow relations.

Integration of the overall continuity equation utilizing the boundary conditions yields

$$\dot{m} = \dot{m}_d = -\frac{\bar{\rho}\nu}{\sigma_\kappa(1+\kappa)}\frac{d\kappa}{dy} \tag{11}$$

The x-momentum equation can be integrated across both layers:

$$\tau = \tau_w + \dot{m}(u - u_w) = \bar{\rho}\nu\frac{du}{dy} \tag{12}$$

Subscript w refers to the packed layer surface. The turbulent kinetic energy is assumed to be dominated by the inhomogeneous terms in the energy conservation equation as is the case in a clean air boundary layer. In other words, the production of turbulent kinetic energy is in balance with its loss:

$$k = \frac{\tau}{\rho(1+\kappa)\sqrt{C_D}}, \qquad C_D = 0.09 \tag{13}$$

It is assumed that the turbulent scale is linear in y, as in a clean air boundary layer, but the constant of proportionality is altered because of the presence of the particles:

$$l = \frac{k_a C_D^{\frac{1}{4}} y}{C}, \qquad k_a = 0.406 \tag{14}$$

The constant C is unity for clean air. It might be expected that the constant C should be greater than unity for a dusty flow because of the dissipative effect of the particles. It would be preferable to have an analysis that goes smoothly to the clean air case, but for now a value of C has to be found from dusty flow data.

Some dimensionless variables are defined in Eq. (15):

$$\tilde{\tau} = \tau/\tau_e, \qquad \tau^* = \tau\tau_w, \qquad \dot{m}^* = \dot{m}u_\tau/\tau_w$$
$$\tilde{k} = \frac{k(1+\kappa_e)\sqrt{C_D}}{u_\tau^2\tau_e^*}, \qquad n = \frac{\dot{m}^*}{k_a\sqrt{\tau_e^*(1+\kappa_e)}} \tag{15}$$

The parameter τ_e is the value of shear at the outer edge of the law of the wall region. The decay of shear that occurs in the outer (law of the wake) region is not included in the Couette flow regime. The method of solution is to change the independent variable from normal distance to shear. Combining Eqs. (11) and (12) leads to

$$\tilde{\tau} = \frac{1 + \dot{m}^*(u/u_\tau - u_w/u_\tau)}{1 + \dot{m}^*(u_e/u_\tau - u_w/u_\tau)} = \left(\frac{1+\kappa_e}{1+\kappa}\right)^{1/\sigma_\kappa} \tag{16}$$

Use of Eqs. (15), (16), and (13) yields an expression for the dimensionless turbulent kinetic energy in terms of dimensionless shear:

$$\tilde{k} = \tilde{\tau}^{1+\sigma_\kappa} \tag{17}$$

Finally, the normal distance can be found in terms of the shear by use of the definition of eddy viscosity in Eq. (1) along with Eqs. (12–16):

$$\frac{y}{y_m} = \exp(\phi), \qquad \phi = \frac{\tilde{\tau}^s - \tilde{\tau}_m^s}{Cns}, \qquad s = \frac{1-\sigma_\kappa}{2} \tag{18}$$

To complete the Couette flow profiles it is necessary to solve the fluidized layer relations. It is again convenient to use the shear as the independent variable instead of normal distance. The result

of integrating the energy equation using the steady-state ablation boundary condition [Eq. (6)] yields

$$\bar{T} = \bar{T}_w \tau_*^\alpha - \frac{F_1}{F_2}\left\{\left(\frac{1}{2} + \Delta\bar{H}\right)\frac{1-\tau_*^\alpha}{\alpha} + \frac{P_1}{\alpha}\left[\ell_n \tau_* + \frac{1-\tau_*^\alpha}{\alpha}\right] + \frac{\tau_*^2 - \tau_*^\alpha}{2(2-\alpha)}\right\} \tag{19}$$

$$\bar{Q} = \left[\frac{5}{2}\bar{T}_w + \Delta\bar{H}\right]\tau_*^\alpha + \frac{P_1}{\alpha}\left(\tau_*^\alpha - 1\right) - \frac{\tau_*^2 - \tau_*^\alpha}{2-\alpha} \equiv \frac{-q_p \dot{m}}{\tau_w^2}$$

$$\bar{T} \equiv T_p(\dot{m}/\tau_w)^2, \qquad \Delta\bar{H} \equiv \Delta H_v(\dot{m}/\tau_w)^2, \qquad \tau_* \equiv \tau_p/\tau_w$$

$$\alpha \equiv (5/2)(F_1/F_2), \qquad P_1 \equiv c_4 F_1 \bar{P}^2, \qquad \bar{P} \equiv P_p/\tau_w \tag{20}$$

The normal distance in the fluidized layer cannot be found in simple analytic form. It is found numerically from Eq. (21):

$$\frac{y}{d} = \frac{\rho_s F_1}{\rho \dot{m}^{*2}} \int_1^{\tau_{*m}} \frac{\sqrt{\bar{T}}}{\tau_*}\, d\tau_* \tag{21}$$

The complete profile in both regions can be found in terms of a single dimensionless variable that can later be related to a particular station through use of the momentum integral. The shear at the matching point τ_{*m} was found to be a convenient parameter, and in the following discussion it will be considered given. From the definitions given previously it can be shown that $\bar{P}$, κ_w, $\dot{m}^*$, u_w/u_τ, and u_e/u_τ depend upon three unknown parameters: κ_m, $\bar{T}_w$, and $\bar{T}_m$. These three parameters are found by utilizing the temperature and heat flux, Eqs. (19) and (20), evaluated at the matching point while utilizing the matching conditions of Eq. (5) and an additional relationship from the mass flux boundary condition of Eqs. (7–10). Solution is found by means of a Newton–Raphson procedure.

V. Momentum Integral

The overall momentum equation for the gas particle flow can be put in the following form:

$$\frac{\partial}{\partial t}\bar{\rho}_e u_e \delta I_1 + \frac{\partial}{\partial x}\bar{\rho}_e u_e^2 \delta I_2 - \bar{\rho}_e \delta I_3 \frac{\partial u_e}{\partial t} - \bar{\rho}_e u_e \delta I_4 \frac{\partial u_e}{\partial x} - \delta\frac{\partial P}{\partial x} - \frac{\partial y_m P_p}{\partial x} = \bar{\rho}_e u_e^2\left[\frac{\tau_w}{\bar{\rho}_e u_e^2} + \left(\frac{\bar{\rho}_w \nu_w}{\bar{\rho}_e u_e}\right)\left(1 - \frac{u_w}{u_e}\right)\right] \tag{22}$$

The integrals I_1–I_4 are the same as those defined in Ref. 1. In the present case, however, each integral is divided into an integral over the fluidized layer plus an integral over the turbulent layer. The integrals are given in Eq. (23):

$$I_1 = \int_0^1 \frac{\bar{\rho}}{\bar{\rho}_e}\left(1 - \frac{u}{u_e}\right) dy/\delta, \qquad I_3 = \int_0^1 \frac{\bar{\rho}}{\bar{\rho}_e}\, dy/\delta$$

$$I_2 = \int_0^1 \frac{\bar{\rho}}{\bar{\rho}_e}\frac{u}{u_e}\left(1 - \frac{u}{u_e}\right) dy/\delta, \qquad I_4 = \int_0^1 \frac{\bar{\rho}}{\bar{\rho}_e}\frac{u}{u_e}\, dy/\delta \tag{23}$$

The variation of the gas density across the boundary layer can be neglected for the subsonic wind tunnel. For other situations it can usually be assumed that the variation in particle density is much stronger so that the gas density variation can be ignored. Note that δI_1 is the displacement thickness, whereas δI_2 is the momentum thickness for the dusty boundary layer.

VI. Effective Particle Size

It is common practice to determine the fraction less by weight as a function of particle diameter from sieve data. Such a plot is presented in Fig. 2 for a sample of white sands missile range (WSMR) soil.[3] The fraction F can be thought of as an integral of a distribution function $\phi(u)$ over the entire range of particle sizes such that

$$F = \int_0^u \varphi(u_1)\, du_1, \qquad 1 = \int_0^\infty \varphi(u_1)\, du_1, \qquad u = \beta d \tag{24}$$

The constant β is chosen such that $F(\infty)$ is unity. As indicated in Fig. 2, the lower and upper limits for a real soil are from some small finite value to some large finite value. The function F can be broken up into N bins of width Δu. The mass fraction associated with the ith bin is given by Eq. (25):

$$Y_i = \int_{u_i}^{u_i + \Delta u} \varphi(u_1)\, du_1 \tag{25}$$

Other properties can be defined for the bins analogous to a multicomponent fluid:

$$\frac{1}{m} = \sum_{j=1}^{N} \frac{Y_j}{m_j}, \qquad X_i = \frac{Y_i m}{m_i}, \qquad m_i = \frac{\rho_s \pi d_i^3}{6} \tag{26}$$

where X_i is the number fraction associated with the ith bin.

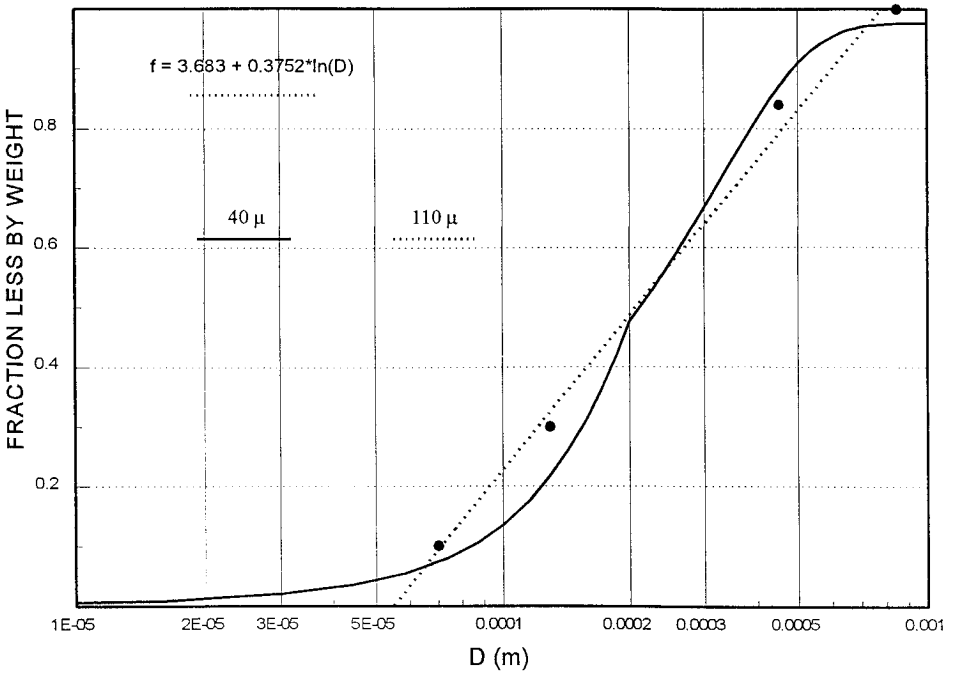

Fig. 2 Use of WSMR sieve data to find effective diameter.

A mass average diameter could be defined from the measured distribution, but the effective diameter should depend upon the manner in which the diameter affects the conservation equations. In the case of velocity lag, the diameter would be introduced through the drag coefficient that depends upon the particle diameter. Velocity lag has been neglected, however, based on the data of Batt et al.[3] The only way the diameter has been introduced in the conservation equations is through the transport properties of the fluidized layer. If it is assumed that all fluidized layer transport properties are affected in the same way by the presence of a distribution of particle sizes, then the effective diameter for the fluidized layer can be obtained by examining the viscosity of the multicomponent system. It is convenient to determine the effective diameter through use of the viscosity of a pure single component fluid with a reference diameter d_r. Because of the good communication between colliding particles of different sizes, it can be assumed that particles of all sizes have the same temperature T_p^*. The energy of the mixture T_p and the reference substance T_{pr} are given by

$$T_p = \sum_{i=1}^{N} \frac{Y_i k T_p^*}{m_i}, \qquad T_{pr} = \frac{T_p m}{m_r}$$
$$\frac{m_r}{m} = \sum_{i=1}^{N} Y_i \left(\frac{d_r}{d_i}\right)^3 \tag{27}$$

The effective diameter of the multicomponent mixture is related to the pure substance of reference diameter d_r by

$$d = d_r(\mu/\mu_r)\sqrt{(m/m_r)} \tag{28}$$

For a multicomponent mixture the viscosity coefficient depends upon the concentrations, and therefore the results of an accurate kinetic theory would be very complicated. A useful semi-empirical formula has been worked out for molecular multicomponent species.[11,12] Upon normalizing this expression with μ_r and estimating the binary diffusion coefficients, the formula can be put in the form given in Eq. (29):

$$\frac{\mu}{\mu_r} = \sum_{i=1}^{N} \frac{X_i\sqrt{(d_r/d_i)}}{X_i + 0.408\sum_{\substack{j=1\\ j\neq i}}^{N} X_j(1+d_j/d_i)^2/\sqrt{1+(d_i/d_j)^3}} \tag{29}$$

Equations (27) and (29) can be used in Eq. (28) to define the effective diameter. The results are indicated in Fig. 2. When the normal distribution is used, the long tail at low diameters is emphasized. This occurs because of the large number fractions associated with that region, which leads to a diameter of only 40μ. When the cutoff distribution is used, the effective diameter is 110μ for the WSMR sample. It is believed that the latter is more realistic and will be used for all of the calculations that will be presented for this soil.

VII. Effective Schmidt Number

Batt et al. presented curvefits of their data for velocity and dust density as a function of normal distance above the soil bed. These data were combined to show the variation of the measured air mass fraction as a function of velocity in the dusty boundary layer. When these data were extrapolated to the surface, there was an apparent finite surface velocity. It was found that a good collapsing of the data occurred when the apparent surface velocity was subtracted from the local velocity for each run. The results are shown in Fig. 3. The data points are shown for eight of Batt et al.'s runs with WSMR soil. Each point corresponds to a calculation from Batt et al.'s curvefits with normal distance eliminated and the apparent surface velocity subtracted rather than the original data points used to construct the curvefits. Notice that all of the data falls in a narrow band on this linear plot. Also shown in Fig. 3 are least-squares power law fits to the data of each run. For large values of $\dot{m}^* u_e/u_\tau$ Eq. (16) becomes of the form plotted in Fig. 3. It can be shown that the constant a should be slightly larger than unity. A value of κ_e larger than zero would tend to make a less than unity, but this tendency is

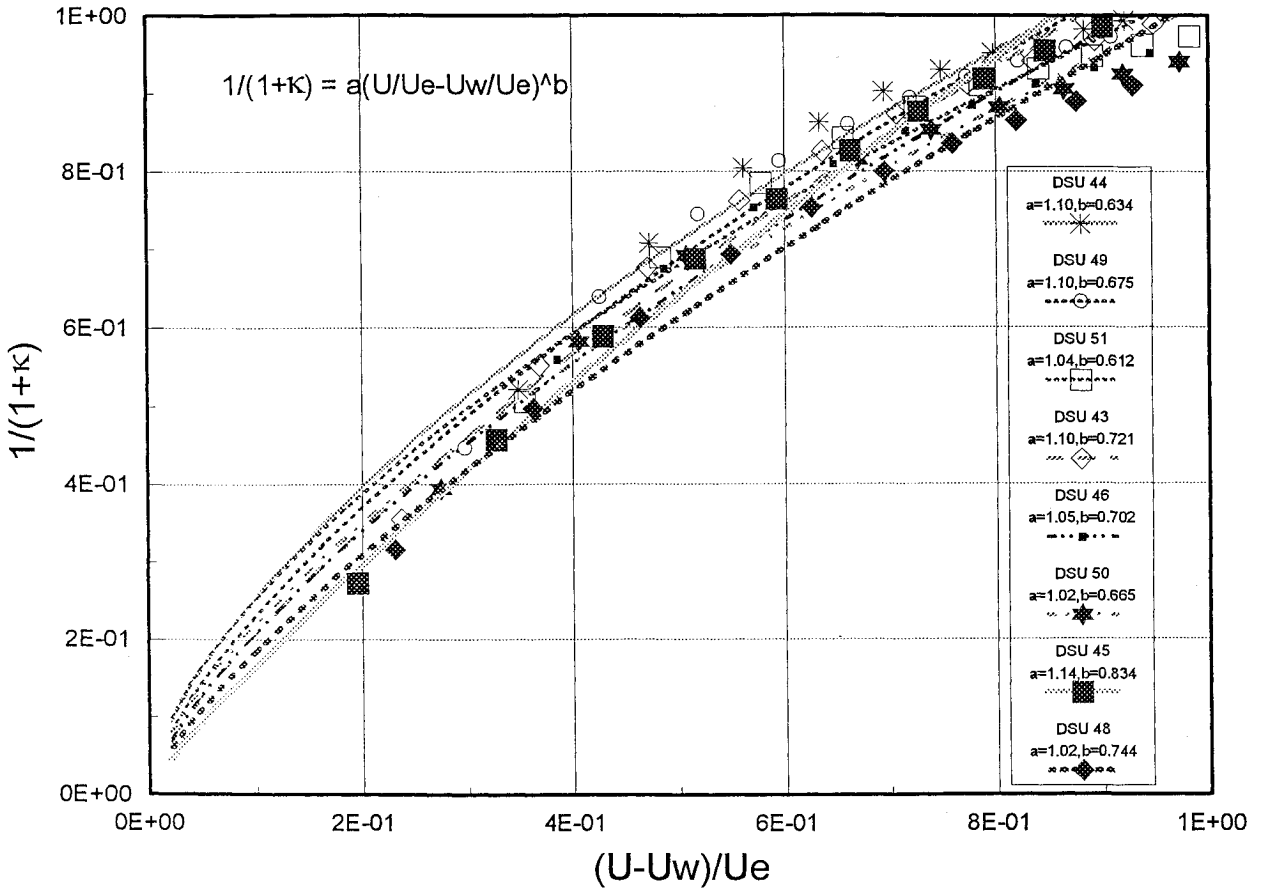

Fig. 3 Power law fits to profiles from wind tunnel data.

overcome by the finite surface velocity that has the opposite effect. From the theoretical distribution [Eq. (16)] in the large mass flux limit the constant b can be identified with the Schmidt number σ_κ. An average value of 0.7 was taken as the Schmidt number. This is a reasonable value because it is expected to be close to but less than unity consistent with the experimental observation that the dust density boundary layer was thicker than the velocity boundary layer.

VIII. Momentum Integral Solutions

The value of the constant C in the turbulence scale [Eq. (4)] was varied to get a good fit to the wind-tunnel data. A value of 4.0 was found to be satisfactory. A comparison with data of the velocity layer thickness computed with this value of the constant is presented in Fig. 4. The calculations were made at constant values of dimensionless fluidized energy, $DH(\Delta H_v/u_e^2)$. It can be seen that these calculations were insensitive to DH and that the slope of the data and the prediction are in good agreement.

The corresponding variation of normalized mass loss with layer thickness is presented in Fig. 5. The strong drop off in mass loss with layer thickness that was observed is also contained in the predictions. Unlike Fig. 4, however, there is a significant variation with DH. The range of DH that was chosen appears to account for most of that which is physically possible. The low DH value of 0.001 is about where the surface particle density is so high that the particles would have to touch. At the other extreme rarefied flow effects begin to occur. It can be seen that the mass loss drops off extremely rapidly under these conditions. If the relationship between wind-tunnel velocity and DH is monotonic, the highest DH would correspond to velocities lower than any of the wind-tunnel

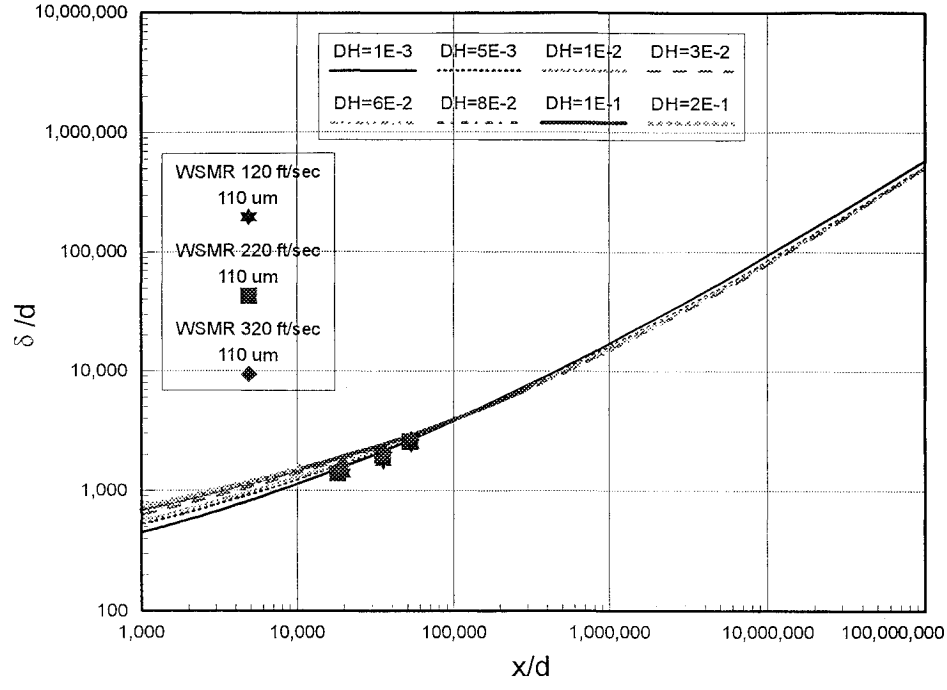

Fig. 4 Comparison of boundary layer thickness with data.

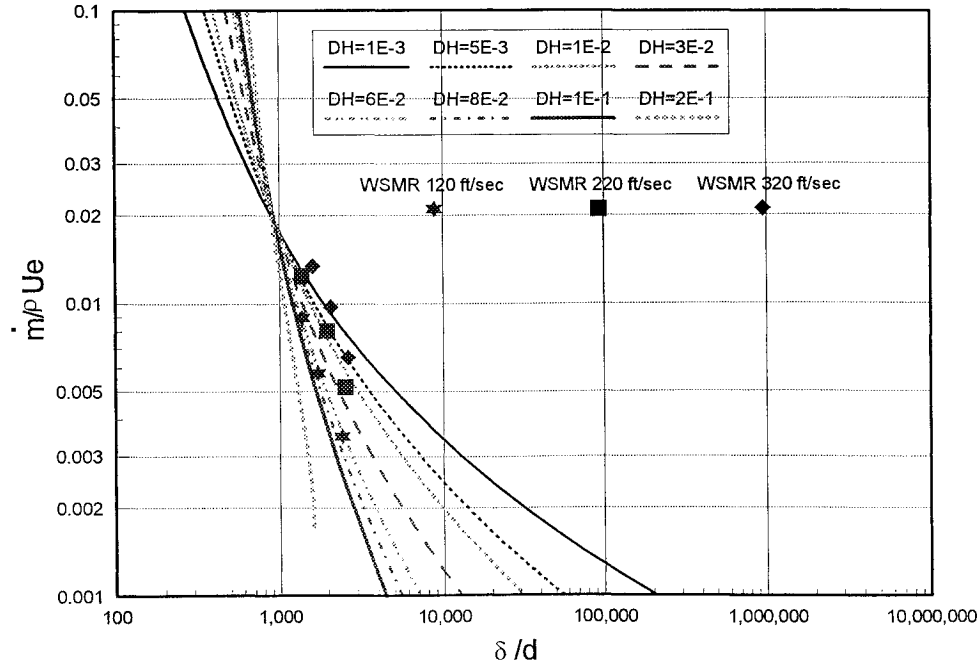

Fig. 5 Comparison of mass loss with data.

runs. Thus it appears that this result is reminiscent of Bagnold's[13] minimum velocity for lofting.

To use the results in matching to a hydrocode it is necessary to find some relationship between DH and some observed quantity in the data. Wind-tunnel velocity appears to sort out the data in an order opposite to DH. An attempt was made to quantify this relationship from the data shown in Fig. 5. The shape of the fit of DH as a function of edge velocity that was chosen takes into account the observation that at large tunnel velocities the corresponding predictions appear to be limited by particle touching at the surface. At low velocities the value of DH is limited because of rarefied flow conditions.

The remaining results needed for matching to a hydrocode are the dependence on layer thickness with fluidization energy as a parameter of mass loss, surface velocity, and surface particle density as well as the integrals I_1–I_4. For each value of DH the variation with layer thickness was fit using the TableCurve™ curvefitting software. The results produced a separate Fortran program for each curve. These were then incorporated as subroutines in the main program for matching to the hydrocode.

IX. Interface of Sweep-Up Model to MAZe Hydrocode

A method has been developed for using the results of this analysis in a subroutine to furnish the shear and mass flux at the first nodal point in the multiphase adaptive zoning (MAZe)[14,15] hydrocode as a function of time. First the boundary-layer thickness is obtained from the time-dependent momentum integral, Eq. (22). The edge properties required in this equation are interpolated from the hydrocode profiles and the curvefits are used for the surface properties and integrals. For an explicit calculation method, solution of the time-dependent boundary-layer momentum equation has convergence criteria that usually require smaller time steps than the hydrocode. Rather than impose this condition on the hydrocode, the hydrocode conditions are held constant for the subgrid calculation until the next hydrocode time step is reached.

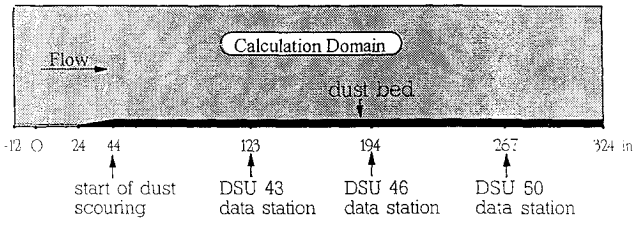

Fig. 6 Calculation domain for wind tunnel dust sweep-up simulations.

The procedure used to interface the sweep-up model to the hydrocode was designed to accommodate either structured or unstructured hydrocode meshes of arbitrary cell shape. To achieve this goal, a rectangular, structured overlay mesh was selected as a means to transmit information between the hydrocode and sweep-up model. For each cell in the structured overlay mesh, the variables air density, air velocity, and dust density (or κ) are interpolated from the hydrocode mesh onto the overlay mesh cell centers. Note that this overlay mesh must encompass the entire dusty boundary layer. The sweep-up model subroutines are then called, and the mass fluxes at the lower boundary (and surface shear if desired) are calculated. The mass fluxes and surface shears are then interpolated back onto the hydrocode mesh to be applied at the lower boundary in the appropriate hydrocode subroutines.

X. Simulation of Wind-Tunnel Experiments

As a final test of the sweep-up model, the MAZe code was used to simulate a series of the laboratory wind-tunnel experiments of Batt et al.[3] as summarized in Table 1. The model was used "as is" without further adjustment of constants. Three simulations were performed, with comparisons being made at three downstream locations, corresponding to the nine individual experiments. These represent all of the experiments done with the sieved WSMR-S soil type by Batt et al.[3] The simulations used an average value for each nominal velocity (107.8, 214.7 and 323.3 fps). The actual experimental average bed lengths were used for comparing the simulations to the experiments, however.

The computational domain is sketched in Fig. 6. Three of the downstream locations for data comparison are shown as examples, although these change slightly for each experiment.

Table 1 List of experiments and simulations

DSU number of Batt	Experimental edge Velocity, fps	Simulation edge Velocity, fps	Average bed length, ft/in.
44	95	107.8	7/1
49	120	107.8	12/8
51	108	107.8	19/0
43	218	214.7	6/7
46	227	214.7	12/6
50	199	214.7	18/7
45	326	323.3	7/1
48	333	323.3	12/10
52	311	323.3	19/0

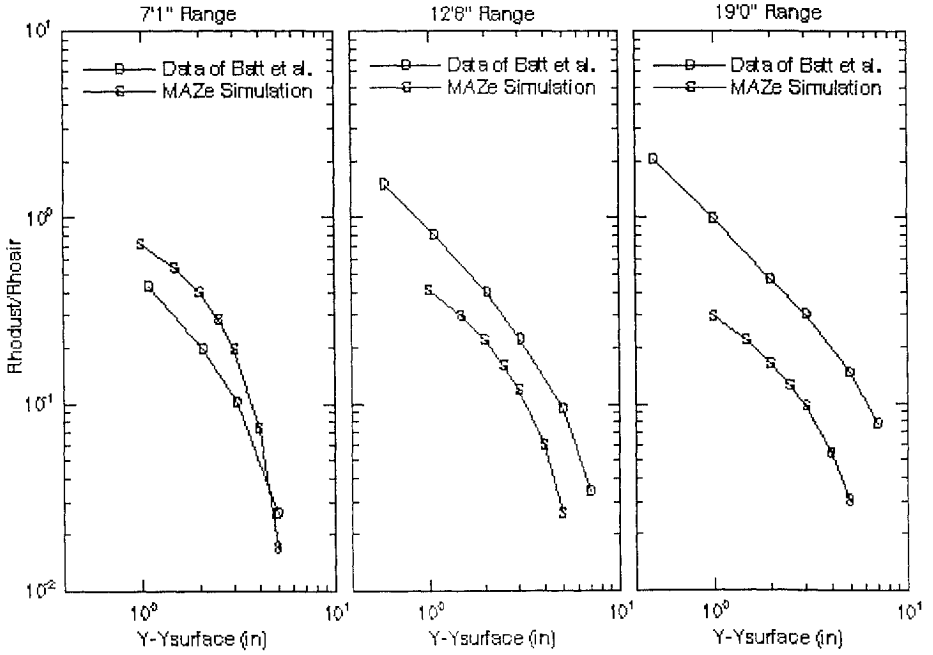

Fig. 7 Comparison of experimental and simulation dust loading (κ) profiles for 100 fps nominal velocity.

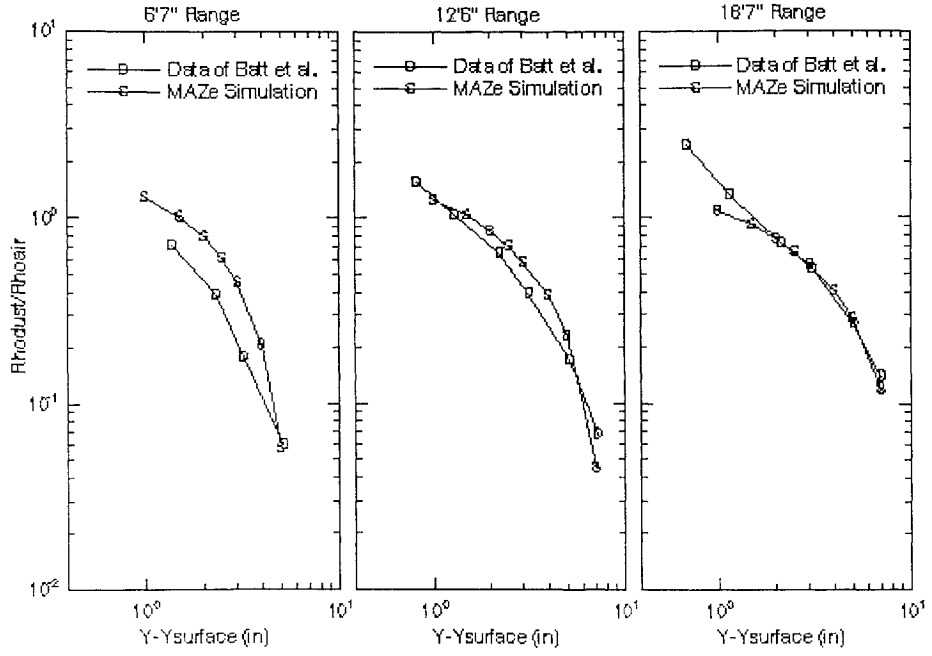

Fig. 8 Comparison of experimental and simulation dust loading (κ) profiles for 200 fps nominal velocity.

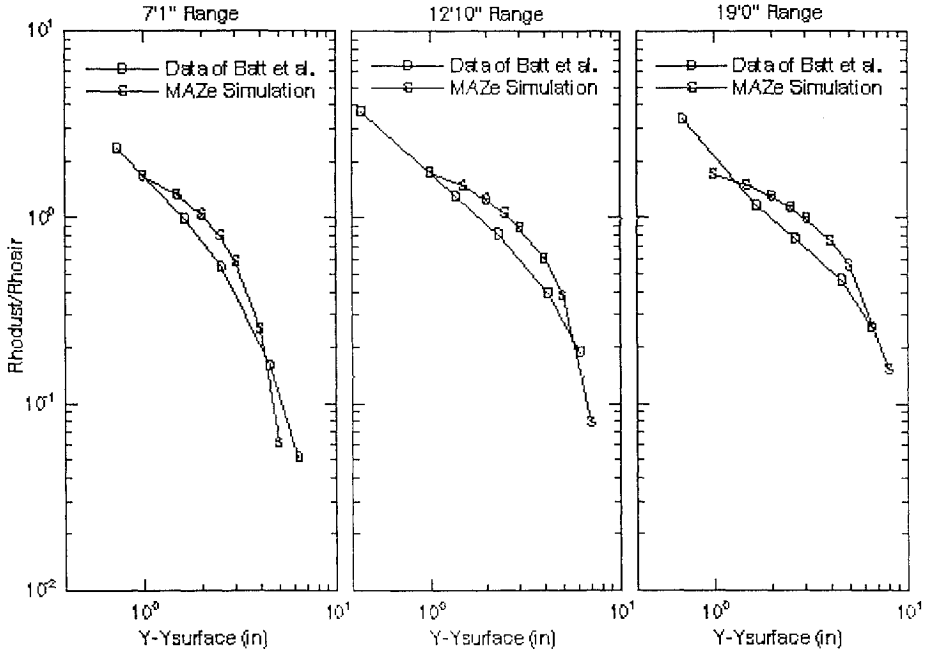

Fig. 9 Comparison of experimental and simulation dust loading (κ) profiles for 300 fps nominal velocity.

The features of the MAZe wind-tunnel simulations are 1) two-dimensional planar, 2) dust scoured from flat lower boundary, 3) simulation started by imposing freestream velocity at left-hand boundary, 4) minimum computational zone size: 0.5 in. high by 4 in. long, and 5) calculation run until steady state was reached (350 ms).

Figures 7–9 show comparisons of experimental and calculated dust loading profiles for the nine cases listed in Table 1. Here the experimental data points are shown by the symbols connected by straight lines. The simulation profiles show values at selected heights, also connected by straight lines. In general, the simulated profiles show good agreement with the experimental profiles, although the simulation profiles tend to show a more rapid decrease in κ with height than the experiments. Also, for the 100 fps nominal velocity particularly, the simulation shows a more rapid decrease in κ with downstream distance than the experiment. This low velocity regime has relatively little relevance to the nuclear blast application, however.

Figure 10 shows plots of $\dot{m}/\rho u_e$ vs downstream distance for the three nominal velocities. The plateau at the upstream end of the simulation curves is due to the fact that the model solution possesses a singularity at the leading edge of the dust bed, and so the solution was ignored near there. For clarity, curvefit to the experimental data done by Batt et al.[3] is shown rather than the data itself. Note that the closest experimental data point to the leading edge of the dust bed was about 35 in. downstream, so for $X-Xle$ less than this value the curvefit to the data is an extrapolation. Overall the agreement is reasonable, although the simulation shows higher values of $\dot{m}$ than the extrapolated curvefit to the data for $X-Xle < \sim 40$, whereas the simulation shows somewhat lower values than the data for $X-Xle > \sim 40$. The simulation also shows a more rapid decrease in $\dot{m}$ with range than the data for $\sim 40 < X-Xle < \sim 90$ in.

Comparisons of simulated and experimental velocity profiles for the 200-fps nominal velocity are shown in Fig. 11. The simulated velocity profiles become somewhat higher than the experimental

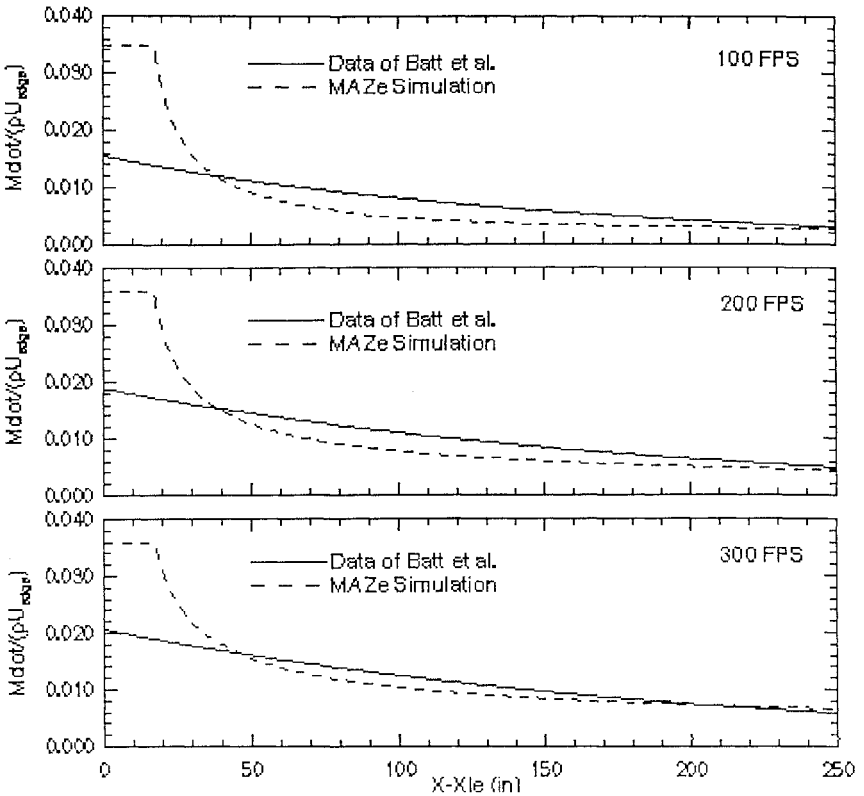

Fig. 10 Comparison of experimental and simulation normalized mass lofting vs streamwise distance (curve-fit to data is shown).

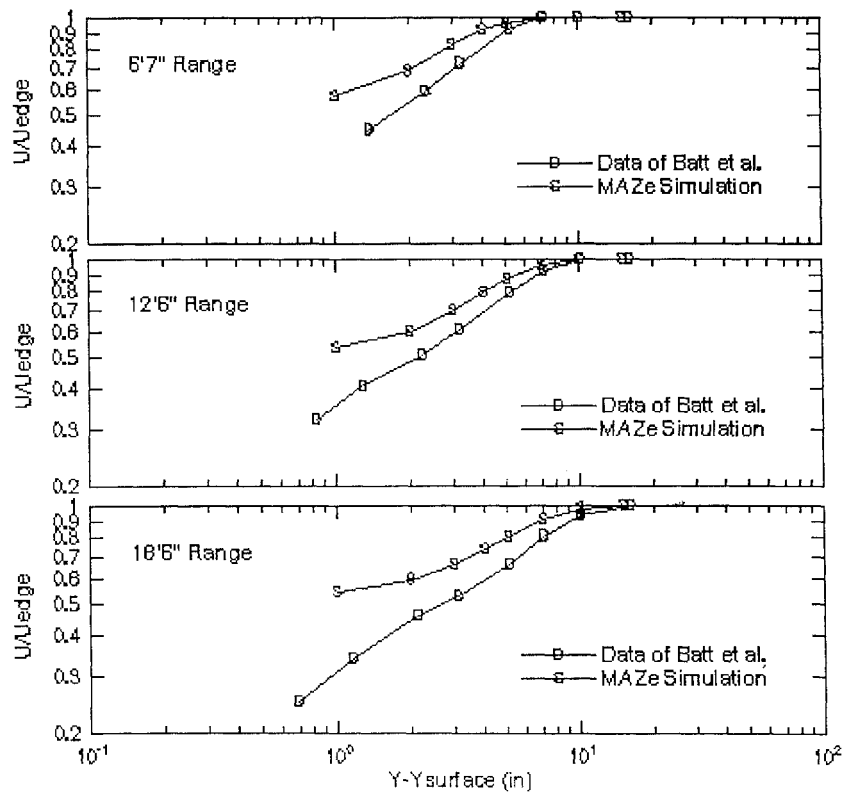

Fig. 11 Comparison of experimental and simulation normalized velocity profiles for 200 fps nominal velocity.

profiles as the wall is approached. This difference may be due to insufficient resolution of the boundary layer in the hydrocode. Note also that since the hydrocode does not model particle-particle impacts explicitly, it is not valid in the high-density fluidized layer near the ground. Therefore, even if the hydrocode resolution were increased, it would not be expected to produce the right velocity profile in the near-wall region.

The results of a study of the effect of hydrocode zoning on κ profiles are shown in Fig. 12 for the nominal 200-fps velocity case at the 12 ft 6 in. downstream distance. The data are shown along with calculated profiles for 2-, 4-, and 8-in. zone sizes (the 0.5-in. zone size data are shown in Fig. 8). All of the simulations produce reasonable agreement with the experiment, at least at the lowest mesh point. This reasonable agreement is not surprising, since κ at

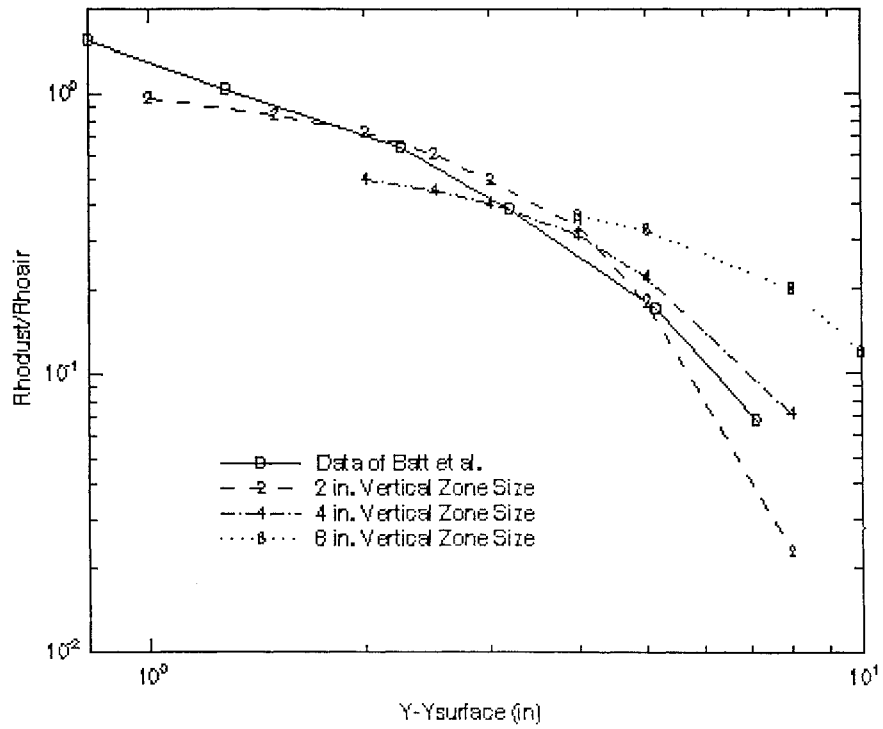

Fig. 12 Effect of hydrocode zone size on dust loading factor (κ) profiles for 200 fps nominal velocity, 12 ft 6 in. range.

the lowest mesh point is inversely proportional to the zone height, assuming a constant mass flux. Thus plotting κ at the lowest mesh point vs zone height produces a line with a slope-1, which approximately corresponds to the slope of the experimental data, up to some limit where dust loading begins to decline more rapidly with height. One somewhat surprising result of this study, however, is that the calculated mass flux is essentially constant when there are at least ~2 zones vertically in the boundary layer, i.e., the model does not require particularly fine resolution of the boundary layer to calculate mass flux. For the present case, zone heights greater than about 8 in. (~1 zone in the boundary layer) produce the inevitable overdiffusion of dust upward at the higher mesh points. Thus, the ultimate limitation in accuracy of the vertical profiles of dust density in the hydrocode is due to overdiffusion due to large cell size, rather than inaccurate mass fluxes calculated in the sweep-up model. In the limit when there is no resolution of the boundary layer in the hydrocode, it is recommended that no dust be put into the hydrocode and the dust profiles calculated by the subgrid model be used as an estimate below the first mesh point.

XI. Conclusions

Introduction of the energy of fluidization in this analysis appears to be a useful concept for characterizing soils or surface composition. The variation of this parameter with freestream velocity for WSMR soil has been established. It is hoped that such a correlation can be obtained for other real surfaces of interest.

In addition to determining the energy of fluidization, the wind-tunnel tests have been used to determine some unknown parameters in the dusty turbulent boundary layer of the subgrid model. These parameters include the effective Schmidt number and the increase in the turbulent dissipation due to particles characterized by the constant C. The strong decay in mass lofting with distance predicted by the model was very well correlated with the experiments. This has important implications for scaling to air blasts that may be several orders of magnitude larger than the wind-tunnel tests.

Several improvements have been made in the two layer model that was introduced in Ref. 2. It has been shown how to obtain an effective diameter for the particles when a spectrum of particle sizes is present. For the WSMR dust a value of 110μ appears to be a reasonable estimate. The concept of net mass flux at the surface resulting from the flux leaving and the flux striking the surface was introduced by analogy with molecular substances. This concept allowed relaxation of an arbitrary specification of the matching point between the turbulent and fluidized layers. Important improvements were made in the energy balance conditions at the interfaces, including the introduction of the energy of fluidization. An allowance was also made for the occurrence of slip flow when the mean free path in the fluidized layer becomes large. This helps to characterize the low velocity regime in which the mass lofting drops off extremely rapidly.

A method has been developed for matching this boundary-layer analysis with a hydrocode calculation. The current sweep-up model was implemented in the MAZe hydrocode and used to simulate a series of wind-tunnel dust sweep-up experiments. The model produced good overall agreement with experimental mass lofting rates and vertical dust loading profiles measured in a wind tunnel by Batt et al. at velocities from ~100 to ~300 fps for sieved, incohesive soils. The mass lofting calculated by the model was relatively insensitive to hydrocode zoning in the dust boundary layer, provided at least ~2 zones spanned this layer.

Further work needs to be done to apply the method to other real surfaces of interest.

Appendix: Transport Properties (Ref. 10)

$$\eta = \frac{1}{2}(1+e), \qquad A1 = \frac{5\pi^{\frac{1}{2}}}{96\eta(2-\eta)}$$

$$A2 = 8\eta/5, \qquad A3 = A2(3\eta - 2), \qquad A4 = A2/\pi^{\frac{1}{2}}$$

$$B1 = \frac{25\pi^{\frac{1}{2}}}{16\eta(41-33\eta)}, \qquad B2 = \frac{12\eta}{5}$$

$$B3 = B2\eta(4\eta - 3), \qquad B4 = \frac{64(41-33\eta)\eta^2}{25\pi}$$

$$C1 = \frac{48(1-\eta)\eta}{\pi^{\frac{1}{2}}}, \qquad g = \frac{(1-\nu/2)}{(1-\nu)^3}$$

$$F1 = (A1/g)(1 + A2\nu g)(1 + A3\nu g) + A4g\nu^2$$

$$F2 = (B1/g)[(1 + B2\nu g)(1 + B3\nu g) + B4(\nu g)^2]$$

$$F3 = \nu + 4\eta g\nu^2, \qquad F4 = C1g\nu^2$$

Acknowledgments

Work reported herein was performed by the Titan Research and Technology Division of the Titan Corporation during the period September 24, 1991, through December 24, 1993, for the Defense Nuclear Agency (DNA) under Contract DNA001-91-C-0154. The authors would like to acknowledge the contributions of several others to this work. The authors wish to thank Eric Baum of TRW for numerous in-depth discussions of the physical problem, Richard Batt of TRW for detailed discussions about data, and Richard J. Schlamp of Titan Corporation for code implementation and debugging. The work was supported and monitored by Charles Gallaway and Mark Byers of DNA/SPWE.

References

[1]Denison, M. R., and Baum, E., "Non-Ideal Airblast Subscale Phenomenology Experimentation Program, Volume 1—Boundary Layer Analysis," Defense Nuclear Agency, DNA-TR-87-3-VI, Alexandria, VA, Sept. 1986.

[2]Denison, M. R., "Non-Ideal Airblast Phenomenology Experiments Program, Volume VI—A Two Layer Model of Dust Lofting," Defense Nuclear Agency, DNA-TR-89-48-V6, Alexandria, VA, Feb. 1990.

[3]Batt, R. G., Petach, M. B., Peabody, S. A., II, and Batt, R. R., "Experimental Investigation of Vegetation and Dust Sweep-Up," Defense Nuclear Agency, DNA-TR-92-53, Alexandria, VA, Jan. 1993.

[4]Ausherman, D. R., "Initial Dust Lofting: Shock Tube Experiments," Defense Nuclear Agency, DNA3162F, Alexandria, VA, Sept. 1973.

[5]Batt, R. G., Kulkarney, V. A., Behrens, H. W., and Rungaldier, H., "Non-Ideal Airblast Phenomenology Program, Vol. 3, Laboratory Scale Shock Tube Experiments," Defense Nuclear Agency, DNA-TR-87-3-V3, Alexandria, VA, Dec. 1986.

[6]Denison, M. R., and Baum, E., "Engineering Research Support to Defense Nuclear Agency ICBM Basing Program, Volume III—Dusty Boundary Layer Modeling," Defense Nuclear Agency, DNA-TR-84-355-V3, Alexandria, VA, Dec. 1984.

[7]Hartenbaum, B., "Lofting of Particulates by a High Speed Wind," Applied Theory, Inc., Defense Nuclear Agency, DNA 2737, ATR-71-25, Alexandria, VA, 1971.

[8]Mirels, H., "Blowing Model for Turbulent Boundary Layer Dust Ingestion," *AIAA Journal*, Vol. 22, No. 11, 1984.

[9]Rosenblatt, M., Hatfield, D., Hassig, P., and Gaj, R., "Real Surface Airblast Calculations Using a Modified Mixing Length Model (Case H-503; 1Mt SHOB = 200 ft/Kt1/3)," Non-Ideal Airblast Environment Review, RDA, Marina del Rey, CA, Jan. 1985.

[10]Lun, C. K., Savage, S. B., Jeffrey, D. J., and Chepurniy, N., "Kinetic Theories for Granular Flow: Inelastic Particles in Couette Flow and Slightly Inelastic Particles in a General Flowfield," *Journal of Fluid Mechanics*, Vol. 140, 1984, pp. 223–256; see also Gidaspow, D., *Multiphase Flow and Fluidization: Continuum and Kinetic Theory Descriptions*, Academic, San Diego, CA, 1994.

[11]Hirschfelder, J. O., Curtiss, C. F., and Bird, R. B., *Molecular Theory of Gases and Liquids*, Wiley, New York, 1954.

[12]Penner, S. S., *Chemistry Problems in Jet Propulsion*, Pergamon, New York, 1957.

[13]Bagnold, R. A., *The Physics of Blown Sands and Desert Dunes*, Methuen, London, 1941.

[14]Hookham, P. A., Hatfield, D. W., and Rosenblatt, M., "Calculation of the Interaction of Three Spherical Blast Waves over a Planar Surface with an Adaptive-Grid TVD Code," *Proceedings of the 18th International Symposium Shock Waves* (Sendai, Japan), edited by K. Takayama, Springer–Verlag, Berlin, 1992, pp. 1099–1106.

[15]Hookham, P. A., et al., "Non-Ideal Surface Airblast and Vehicle Loads Predictions in Support of Rail Garrison," Defense Nuclear Agency, DNA-TR-90-197, Alexandria, VA, 1991.

[16]Batt, R. G., and Peabody, S. A., II, "Dust Sweep-Up Experiments," Defense Nuclear Agency, Defense Nuclear Agency, DNA-TR-94-117, Alexandria, VA, 1994.